Stability, Electronic, Elastic, and Mechanical Properties of Graphene/TiO_2 Heterostructure — Theoretical Study Using DFT

W.S. Rasool and M.A. Al-Kaabi*

Kerbala University, College of Science, Department of Physics, Al-jahiz, K17-56001, Karbala, Iraq

Received: 03.09.2025 & Accepted: 23.12.2025

Doi: 10.12693/APhysPolA.149.38 *e-mail: mohammed.alkaabi@uokerbala.ed.iq

In this study, we conduct an in-depth exploration of the stability, mechanical, elastic, and electronic properties of a two-dimensional graphene/titanium dioxide (GR/TiO_2) heterostructure using density functional theory calculations. After geometry optimization, we confirm that the individual structures are stable, with respective lattice parameters of $a = b = 12.33$ Å and vacuum parameter of $c = 13.60$ Å for graphene, $a = b = 11.86$ Å and $c = 29.83$ Å for TiO_2, and $a = b = 12.19$ Å and $c = 15.83$ Å for GR/TiO_2. This stability is further confirmed by formation energy calculations and phonon spectral analyses, which ensure the absence of imaginary modes. It is demonstrated that a strong Ti–O–C type chemical bond is established between the two components, leading to strong electronic coupling and a notable enhancement of optical response in the visible range, thus reinforcing the capabilities of TiO_2 for photovoltaic and photocatalysis applications. Regarding mechanical properties, we determine Young's modulus, shear modulus, and Poisson's ratio based on elastic constants, thus confirming the mechanical stability and strength of the hybrid material under deformation. Band structure analysis reveals that the GR/TiO_2 heterostructures exhibit indirect bandgap semiconductor behavior, with a reduced gap of 0.88 eV. This, in fact, is in a sharp contrast with the intrinsic gap of 2.932 eV for pure TiO_2. The reduction in the energy gap is corroborated by the density of electronic state calculations, which indicate significant hybridization of states at the interfaces, favorable for efficient charge transport. These results highlight the remarkable potential of the GR/TiO_2 system for next-generation electronic, optoelectronic, and photovoltaic devices, particularly in the context of optimal exploitation of the solar spectrum.

topics: density functional theory (DFT), interface, band structures, elastic constant

1. Introduction

In recent years, graphene-based semiconductor composites have gained significant attention for converting solar energy into chemical fuels and for environmental remediation applications [1]. Heterogeneous semiconductor photocatalysts are advantageous because they can function under ambient conditions while utilizing sunlight, which is a clean and renewable energy source [2]. However, achieving high efficiency, long-term stability, durability, and strong visible-light activity continues to be a major challenge [3]. TiO_2 has played a fundamental role in photocatalysis since the first demonstration of photo-induced water splitting on TiO_2 electrodes [4]. It is widely utilized due to its excellent chemical stability, non-toxicity, low cost, and environmentally friendly nature [5, 6]. TiO_2 is a wide-bandgap n-type semiconductor that exists primarily in three crystalline phases: anatase (bandgap $E_g \approx 3.2$ eV), rutile ($E_g \approx 3.0$ eV), and brookite. Among these, anatase and rutile are most commonly employed in photocatalysis, although their light absorption is largely limited to the ultraviolet region [7–9].

Graphene (GR) — a two-dimensional (2D) carbon allotrope — consists of a single atomic layer arranged in a hexagonal honeycomb lattice and represents the building block of other graphitic materials [10, 11]. Although its theoretical existence was proposed decades ago, its remarkable properties have only recently been experimentally realized, including its exceptionally high theoretical surface area (2630 m^2/g), ultra-high carrier mobility ($\sim 200\,000$ $cm^2/(V\ s)$), Young's modulus in the tera-pascals range, superior thermal conductivity (~ 5000 $W/(m\ K)$), high optical transparency (97.7%), and the ability to sustain extremely high current densities (~ 108 A/cm^2) [12–14].

From a theoretical perspective, numerous studies have focused on modeling GR/TiO_2 interfaces by investigating their electronic, optical, and charge-transfer characteristics [15, 16]. Using an *ab initio*

method, Sivek [17] demonstrated that adsorption of a TiO_2 monolayer on graphene leads to interfacial electronic doping, which depends on the atom closest to graphene (Ti acts as an electron donor, while O as an acceptor). Other theoretical investigations [18–21] have further revealed that coupling Ti, TiO_2, or carbon nanotubes to graphene significantly improves photo-generated charge separation, prolongs carrier lifetimes, and enhances visible-light absorption-critical features for photovoltaic and photocatalytic applications.

The present study is dedicated to an advanced investigation of interfacial effects in GR/TiO_2 heterogeneous systems, with a particular emphasis on their electronic properties and structural stability. To fulfill this objective, advanced modeling approaches using density functional theory (DFT) calculations were implemented and refined.

This work addresses the existing knowledge gap related to hybrid materials, which are difficult to model due to the lattice mismatch and the structural complexity arising from the combination of hexagonal graphene and trigonal TiO_2.

The obtained results offer novel insights into the interfacial mechanisms governing GR/TiO_2 nanocomposites, contributing to the development of next-generation 2D photocatalysts. These materials are tailored to meet future energy demands and align with global efforts toward sustainable energy development and technological innovation.

2. Methodology

As part of this work, DFT calculations were performed to investigate the structural and electronic properties of GR/TiO_2 heterostructures. In this methodology, simulations were carried out using the Cambridge Sequential Total Energy Package (CASTEP) code, a well-established computational tool based on plane-wave pseudopotentials, which is renowned for its accuracy in modeling materials at the atomic scale [22, 23]. Valence electrons were expanded in a plane-wave basis set, while interactions between valence electrons and ionic cores were described using norm-conserving pseudopotentials. This approach represents a mathematical simplification that replaces the explicit treatment of core electrons with an effective potential, thereby facilitating the calculation of valence electron behavior in quantum-mechanical simulations. Exchange–correlation effects were treated within the generalized gradient approximation (GGA) using the Perdew–Burke–Ernzerhof (PBE) functional, which is widely employed due to its robustness in describing complex systems [24, 25].

However, because standard GGA has limitations in accurately capturing the localized Coulomb interactions in the Ti $3d$ states, a DFT+U correction was applied to refine the electronic structure. Following the scheme proposed by Dudarev et al. [26] (see also [27]), the effective on-site Coulomb parameter $U_{\text{eff}} = 4.5$ eV was used (with $U = 4.5$ eV and $J = 0$). Additionally, van der Waals interactions between GR and TiO_2 were incorporated using the DFT-D2 dispersion correction according to the method of Tkatchenko and Scheffler [28]. Geometry optimizations were performed using the BFGS minimization algorithm [29], in which atomic forces and cell stresses are minimized based on Hellmann–Feynman forces and stresses evaluated on the Born–Oppenheimer (BO) surface [30]. (Name 'BFGS' is derived from the first letter of the surnames of Broyden, Fletcher, Goldfarb, and Shanno.)

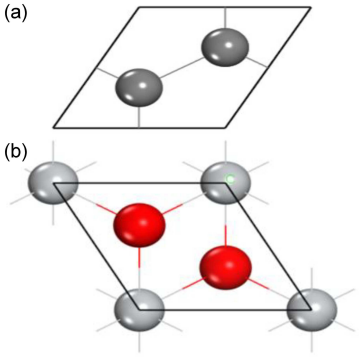

Fig. 1. Model representing the (a) GR and (b) TiO_2 unitcell. The O and Ti atoms are marked in red and grey, respectively. Dark atoms are carbon atoms.

An energy cut-off of 750 eV was chosen to ensure an adequate inclusion of plane waves in the basis set. Geometric structures were optimized until stringent convergence criteria were met: total energy changes smaller than 10^{-6} eV, residual atomic forces below 0.01 eV/Å, maximum atomic displacements less than 0.03 Å, and maximum residual stress of 0.05 GPa.

Integrations over the first Brillouin zone for structural optimizations were carried out using a $3\times3\times2$ k-point mesh. Subsequently, differential charge density analysis was employed to evaluate interfacial charge transfer — a key factor for understanding electronic mechanisms at the interface.

The lattice mismatch between the GR and TiO_2 layers was estimated to be 4.05%, based on their respective lattice parameters along the x and y directions.

3. Results and discussion

3.1. Structural stability and phonon properties

To analyze the physical properties of the GR/TiO_2 system, it is first necessary to understand the structural features of the isolated monolayers.

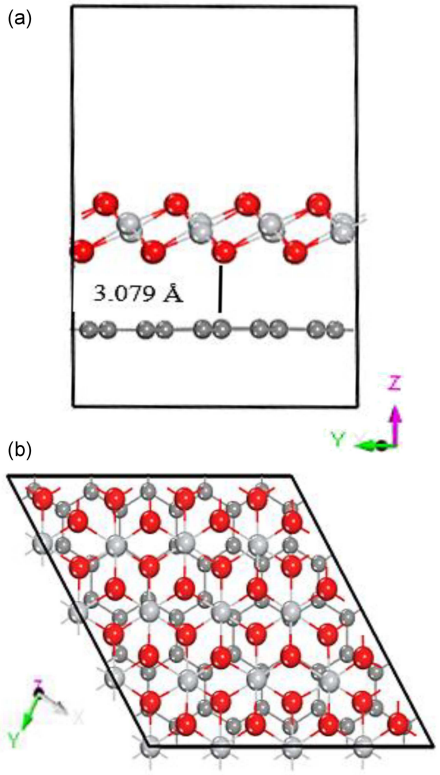

Fig. 2. (a) Top view and (b) side view of a model representing the interface of the GR/TiO_2 bilayer.

Therefore, prior to constructing the heterostructure, we examined free-standing monolayers of TiO_2 and graphene (GR).

The optimized atomic geometries of these monolayers are depicted in Fig. 1. The TiO_2 monolayer crystallizes in the trigonal system belonging to the space group P-3m1 (D3d-3), no. 164. The electronic configurations considered in the simulations were Ti: $3d^2 4s^2$ and O: $2s^2 2p^4$. Structural optimization for TiO_2 was carried out using a $4 \times 4 \times 1$ supercell. The optimized lattice constant of 2.97 Å is in very good agreement with the theoretical value of 2.99 Å reported for a TiO_2 monolayer [31].

In contrast, the graphene monolayer adopts a hexagonal crystal structure associated with the space group P6-mmm (D6h-1), no. 191. The electronic configuration used for carbon was $2s^2 2p^2$. Structural optimizations for graphene were performed on a $5 \times 5 \times 1$ supercell. The resulting optimized lattice constant is 2.47 Å, which is in excellent agreement with the commonly accepted theoretical value for monolayer graphene [32].

The structural parameters were further determined through energy–volume optimization by fitting the data to the Birch–Murnaghan equation of state [33]. For GR/TiO_2, the total energy decreases with increasing volume until a minimum is reached, corresponding to the ground-state minimum energy of −46795.88 eV. The volume corresponding to this minimum, 2037.38 Å^3, is taken as the optimized volume of the system from which the equilibrium lattice constants are extracted.

TABLE I

Lattice constants optimized for TiO_2, graphen (GR), and GR/TiO_2.

		Structures		
		TiO_2	GR	GR/TiO_2
Lattice parameters [Å]	a	11.86	12.33	12.19
	b	11.86	12.33	12.19
	c	29.83	13.60	15.83
Corresponding angle	α	90	90	89.73
	β	90	90	90.20
	γ	120	120	120

The optimized GR/TiO_2 heterostructures are presented in Fig. 2. After relaxation, the in-plane lattice constants for the bilayer structure are $a = b = 12.19$ Å and $c = 15.83$ Å (see Table I). The interlayer distances between C–O and C–Ti are 3.079 Å and 3.80 Å, respectively. These values are slightly larger than those generally reported in the literature; according to the literature, typical C–Ti and C–O separations are about 3.24 Å and 2.99 Å, respectively [34]. Nevertheless, these distances remain within the optimal range for van der Waals interactions [35, 36]. The somewhat larger interlayer spacing in the GR/TiO_2 system can be attributed to the effective covalent radii of the atoms at the interface, leading to an increased separation between the two monolayers [37]. Interlayer distances below 3 Å have also been reported in other TiO_2-based heterostructures [38]. To further evaluate the structural stability of the GR/TiO_2 heterostructure, the formation energy was calculated by comparing the total energy of the combined system with that of the isolated components after full relaxation. The resulting formation energy of −2.93 eV indicates that the van der Waals-bound heterostructure is energetically favorable. This value is close to a previously reported value of −3.15 eV [39]. The similarity between the calculated formation energy and the adsorption energy highlights the importance of van der Waals interactions in governing the stability and properties of the system. In conjunction with the observed interlayer distances, these findings point to a high degree of structural stability and strong physical coupling between the monolayers. The stability is further confirmed by phonon dispersion calculations.

The phonon dispersion curve confirms the dynamical stability of the system under investigation [40]. The absence of imaginary (negative) phonon frequencies throughout the entire Brillouin zone (see Fig. 3) demonstrates the intrinsic vibrational stability of the heterostructure.

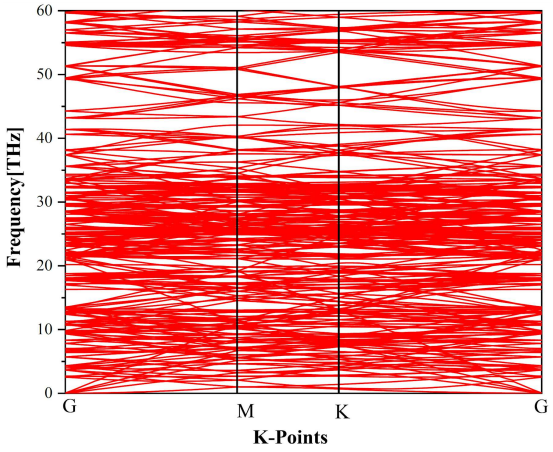

Fig. 3. The phonon dispersion curves for the GR/TiO_2 bilayer.

The GR/TiO_2 supercell, containing 98 atoms, generates a total of 294 phonon branches, i.e., three acoustic modes and 291 optical modes. An overlap between the acoustic and optical branches is observed, which can be attributed to the pronounced differences in atomic masses between the graphene and TiO_2 constituents. This feature reflects the complex vibrational interactions at the interface and underscores the robust nature of the investigated heterostructure.

3.2. Band structure and density of state

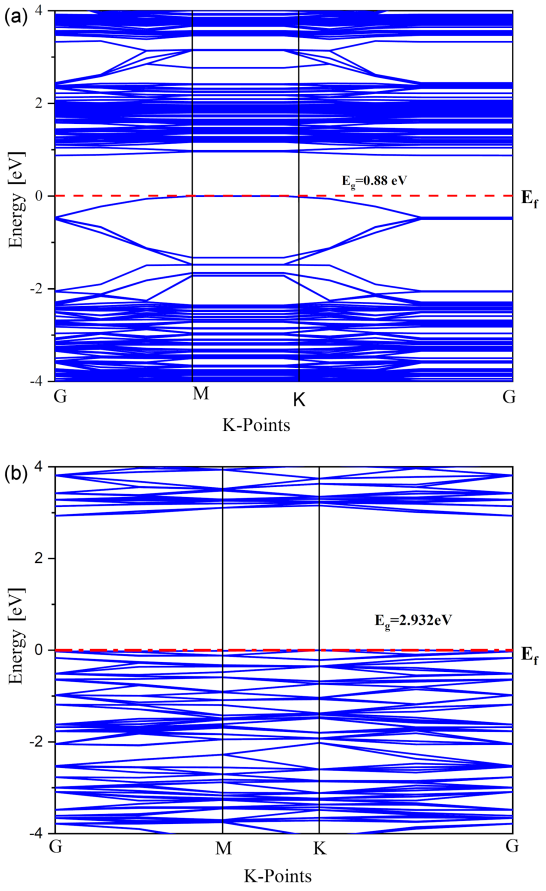

Fig. 4. Band structures for (a) TiO_2 and (b) GR/TiO_2 using GGA + U calculations.

To evaluate the effect of hybridization on the electronic properties of the GR/TiO_2 bilayer, electronic band structures were computed for both the pristine TiO_2 monolayer and the GR/TiO_2 heterostructure. Band gaps were obtained using the GGA-PBE+U functional. The band structures were analyzed along the high-symmetry G–M–K–G path in the Brillouin zone.

For the GR/TiO_2 bilayer, the valence band (VB) maximum is located between the M and K points, whereas the conduction band (CB) minimum is found at the Γ point. The corresponding bandgap (E_g) is about 0.88 eV (Fig. 4b); for comparison, the theoretically value reported is 0.23 eV [41]. In contrast, the TiO_2 monolayer exhibits an indirect bandgap of ≈ 2.932 eV (Fig. 4a).

The substantial narrowing of the bandgap in the composite correlates with a marked improvement in electrical conductivity, which is consistent with various experimental studies [42–45]. The reduced bandgap of GR/TiO_2 facilitates electronic transitions between VB and CB, which is a key factor in explaining the superior photocatalytic performance of the hybrid system relative to the TiO_2 monolayer. The Fermi level is taken as the zero-energy reference level. The charge–carrier separation (in terms of electrons from holes) is more efficient in the GR/TiO_2 bilayer, indicating enhanced photocatalytic activity compared with pure TiO_2. Moreover, the indirect nature of the bandgap in GR/TiO_2 contributes to reducing the recombination rate of photoexcited electron–hole pairs due to the momentum mismatch in the k-space.

In summary, the combination of a reduced bandgap and its indirect character significantly contributes to the enhanced photocatalytic efficiency of the GR/TiO_2 bilayer.

Following a detailed analysis of the electronic band structures of TiO_2 and the GR/TiO_2 heterostructure, Fig. 5a presents the total density of states (DOS) for these systems. The formation of the van der Waals-bound heterostructure induces a noticeable shift of the TiO_2 DOS toward lower energies, indicating a substantial modification in the electronic structure.

The upper part of the valence band is predominantly composed of C 2p and O 2p states, with the O 2p states providing the main contribution, suggesting significant localization of electronic charge around the oxygen atoms. In the lower part of the conduction band, strong hybridization among C 2p, O 2p, and Ti 3d orbitals is observed. This is

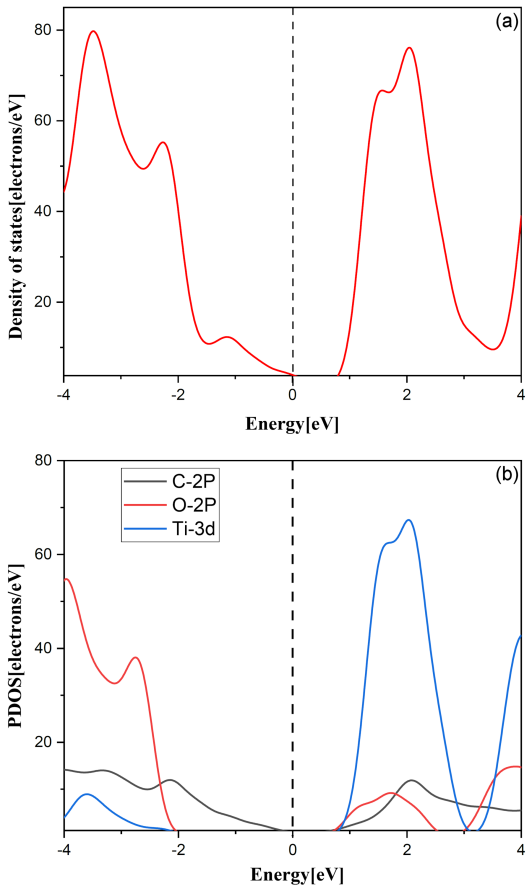

Fig. 5. (a Density of states (DOS) and (b) partial density of state (PDOS) of the GR/TiO_2 heterostructure.

further confirmed by the partial density of states (PDOS) shown in Fig. 5b, where the interfacial oxygen atoms contribute significantly to the upper occupied region of the valence band, as a result of covalent bonding between oxygen and carbon atoms in graphene. Additionally, the contribution of carbon at the bottom of the conduction band is amplified by the C–O–Ti bonding configuration. Experimentally, the presence of oxygen at the interface is known to play a crucial role in improving electron–hole separation and thereby enhancing the catalytic performance of GR/TiO_2 composites [46–48].

Under the influence of visible-light irradiation, electrons residing in the upper valence band can be excited directly from the graphene layers to conduction band states dominated by Ti 3*d* orbitals. This interfacial electron transfer promotes efficient charge separation and suppresses recombination of electron–hole pairs, leading to significantly improved photocatalytic activity.

Hybrid orbitals arising from the combined contributions of Ti 3*d*, O 2*p*, and C 2*p* states can be identified over a wide energy range from −4 to 4 eV, highlighting the complexity and richness of electronic interactions within this heterostructure.

3.3. Differences in electron density

The charge density difference describes how electronic charge is redistributed between the electrocatalyst and the adsorbed intermediates as a result of bond formation and interfacial interactions [49].

The pronounced modification of the density of states of the GR/TiO_2 heterostructure reflects substantial charge transfer between its components. This effect is visualized by the 3D differential charge density shown in Fig. 6, which illustrates the charge distribution in the GR/TiO_2 bilayer.

In this heterostructure, significant charge accumulation occurs above the Ti and O atoms in the TiO_2 layer. In contrast, regions of charge depletion are observed on the lower side of the graphene sheet. This leads to strong variations in the charge distribution across the graphene monolayer; these variations result directly from interfacial interactions. Similar behavior has been reported in other hybrid semiconductor systems, such as CeO_2/RGO and $SrTiO_3$/RGO [50, 51].

This particular charge distribution can be attributed to the very small separation at the interface, especially between the C atoms in graphene and the O atoms at the TiO_2 surface, which promotes strong electrostatic interactions.

To further explore the charge interactions at the GR/TiO_2 interface, a 3D charge density difference analysis was performed with an iso-value

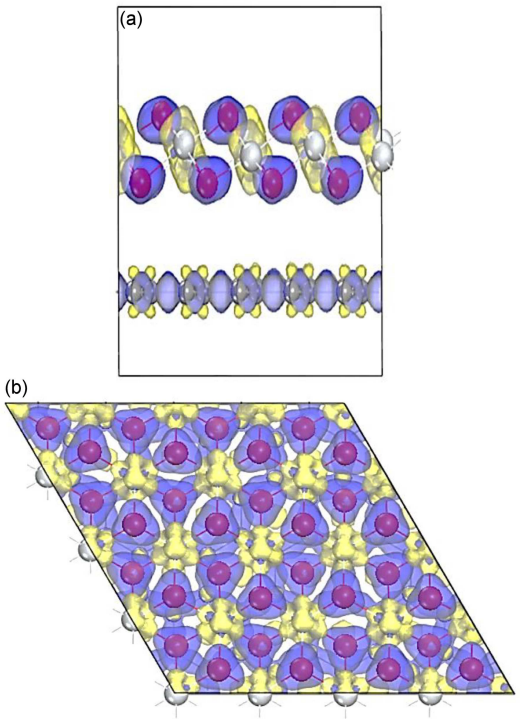

Fig. 6. (a) Top view and (b) side view of 3D charge density differences for GR/TiO_2.

TABLE II

The elastic constant of GR, TiO_2, and GR/TiO_2.

Elastic constants	GR	TiO_2	GR/TiO_2
C_{11}	418.71	283.25	470.83
C_{22}	418.71	283.25	470.83
C_{12}	106.94	64.30	101.184
C_{13}	0.32	5.54	2.50
C_{33}	0.72	10.41	2.31
C_{66}	155.88	109.48	184.82

of $0.1e$ Å^{-3}, enabling precise visualization of the charge accumulation and depletion regions associated with the interfacial bonding.

3.4. Work function

To elucidate the origin of electronic charge transfer, the work functions of TiO_2, GR, and the GR/TiO_2 bilayer were calculated by aligning the Fermi level with respect to the vacuum energy level. The resulting work-function values are 5.007 eV for GR, 8.273 eV for TiO_2, and 4.582 eV for the GR/TiO_2 heterostructure (see Fig. 7a, b, and c), which are in excellent agreement with the values reported in the literature [52].

The direction of interfacial charge transfer in the GR/TiO_2 heterostructure can be readily understood from the differences in these work functions. Nevertheless, the effective amount of charge transferred also depends on other factors, such as the interfacial distance, the nature of the atoms at the interface, their local atomic environment, and their respective electronegativities.

Because the work functions of both TiO_2 and graphene are higher than that of the GR/TiO_2 interface, electrons flow from graphene toward TiO_2 until thermodynamic equilibrium is established. This behavior persists after the two materials are combined, indicating that the intrinsic polarization of the GR/TiO_2 structure plays a key role in generating polarization effects within these heterostructures [53, 54].

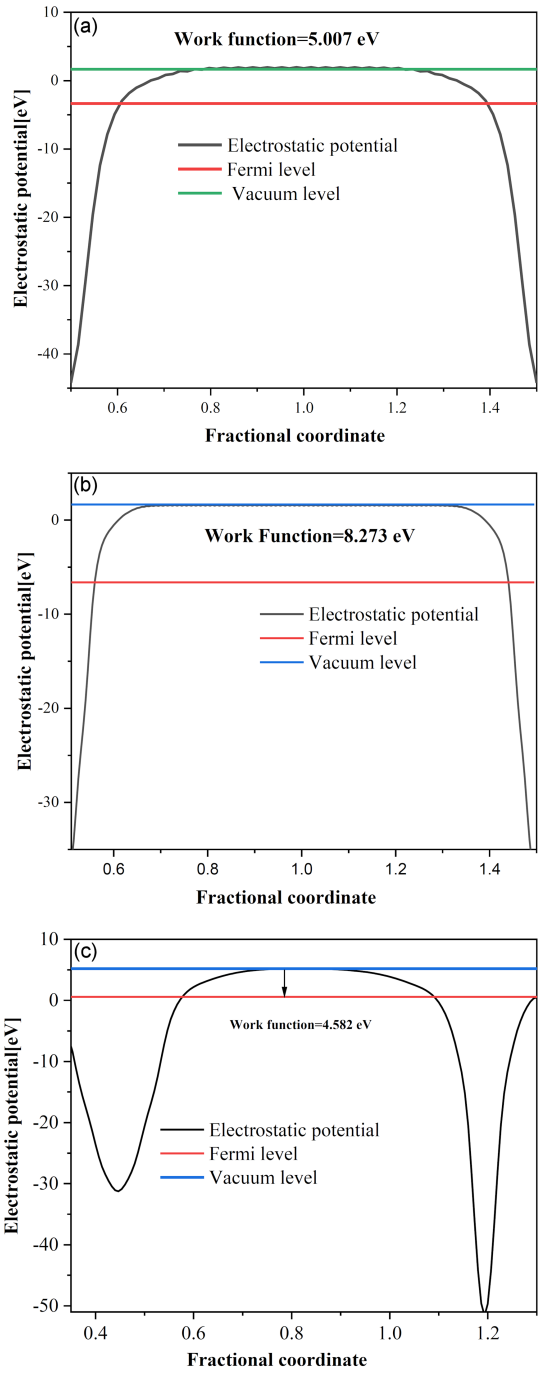

Fig. 7. Work functions of (a) graphene monolayer, (b) TiO_2 monolayer, and (c) GR/TiO_2 bilayer.

3.5. Elastic and mechanical properties

Mechanical stability analysis is crucial for understanding a material's elastic behavior and mechanical response. Elastic constants provide fundamental information on the structural stability and the response of a crystal to external stresses [55]. The elastic constants computed for the graphene monolayer, the TiO_2 monolayer, and the GR/TiO_2 heterostructure are compiled in Table II. All calculated constants satisfy Born's mechanical stability criteria, in particular $C_{11} > 0$, $C_{66} > 0$, $2C_{66} = C_{11} - C_{12}$, and $C_{22} = C_{11}$ [55], thus confirming the mechanical stability of the individual monolayers and the heterostructure.

The values of the elastic constants C_{11}, C_{22}, C_{12}, C_{13}, and C_{66} are presented in Table II. It is observed that the unidirectional elastic constant C_{11} of the GR/TiO_2 heterostructure is higher,

TABLE III

Young's modulus, Poisson ratio, shear modulus, and stiffness [in GPa] of GR, TiO_2, and GR/TiO_2.

Mechanical properties	GR	TiO_2	GR/TiO_2	Ref. [56]
Young's modulus (ϵ)	391.40	268.65	449.08	348
Poisson's ratio (V)	0.26	0.23	0.21	0.29
Shear modulus (G)	155.88	109.48	184.82	125.47
Stiffness (B)	264.46	174.45	284.23	456.36

indicating enhanced stiffness, lower compressibility, and greater resistance to external loading. Analysis also shows that the GR/TiO_2 heterostructure is more compressible than the isolated monolayers when considered individually.

A material's resistance to shear deformation and its hardness are quantified through the shear modulus and Young's modulus, which describe the resistance to shear and to normal stress in the elastic regime, respectively (see Table III). The reference values provide a useful baseline for assessing the mechanical performance of GR/TiO_2. They indicate a material with moderate stiffness and shear resistance, and a Poisson's ratio suggesting relatively good performance under applied stress. These parameters are valuable for benchmarking new materials or composites against established mechanical standards [56].

The similar magnitudes of C_{11} and C_{22} for all three systems indicate that their compressibility and in-plane elastic response along the x and y directions are very close. Moreover, the in-plane elastic constants of the GR/TiO_2 heterostructure are larger than those of the corresponding monolayers, suggesting that van der Waals interactions between layers enhance the in-plane elastic stiffness — a fact consistent with the findings of Peng et al. [57].

4. Conclusions

Two-dimensional (2D) GR/TiO_2 heterostructures were investigated using the PBE-GGA exchange–correlation functional implemented in the CASTEP code. After structural optimization, the energy–volume data were used as the basis for further calculations. Structural stability was confirmed by a negative formation energy, demonstrating the thermodynamic feasibility of the heterostructure.

An internal electric field arises spontaneously within the heterostructure due to the difference in work functions between TiO_2 and GR, which strongly affects charge transfer across the interface.

The mechanical properties of GR/TiO_2 are particularly noteworthy. Young's modulus, shear modulus, stiffness, and other mechanical parameters show enhanced values, reflecting improved structural stability and robustness.

The theoretical model developed in this study introduces a novel approach by employing density functional theory (DFT) to rigorously analyze the interactions at the graphene/titanium dioxide (GR/TiO_2) interface. Specifically, our calculations elucidate the formation of strong Ti–O–C type chemical bonds that directly enhance electronic coupling between the two materials. Unlike previous studies, our detailed investigation of the electronic band structure reveals an indirect bandgap reduction from 2.932 to 0.88 eV, emphasizing the significant hybridization of electronic states at the interface. This unique aspect of our work not only provides precise insights into the charge transport mechanisms but also highlights effective optical response characteristics, which are essential for visible light harvesting. Such detailed analysis paves the way for the design of advanced graphene-based photocatalysts with optimized performance for solar energy applications.

References

[1] Y. Zhang, N. Zhang, Z.-R. Tang, Y.-J. Xu, *ACS nano* **6**, 9777 (2012).

[2] M.-Q. Yang, Y. Zhang, N. Zhang, Z.-R. Tang, Y.-J. Xu, *Sci. Rep.* **3**, 3314 (2013).

[3] W. Wang, B. Cheng, J. Yu, G. Liu, W. Fan, *Chem. Asian J.* **7**, 1902, (2012).

[4] R. Asahi, T. Morikawa, T. Ohwaki, K. Aoki, Y. Taga, *Science* **293**, 269 (2001).

[5] H.-J. Zhai, L.-S. Wang, *J. Am. Chem. Soc.* **129**, 3022 (2007).

[6] J. Chojenka, A. Zarzycki, *Acta Phys. Pol. A* **145**, 147 (2024).

[7] Y. Masuda, G. Giorgi, K. Yamashita, *Phys. Status Solidi B* **251**, 1471 (2014).

[8] Y.-D. Zhou, Z.-Y. Zhao, *Appl. Surf. Sci.* **485**, 8 (2019).

[9] A.N. Banerjee, *Nanotechnol. Sci. Appl.* **2011**, 35 (2011).

[10] M. Sang, J. Shin, K. Kim, K.J. Yu, *Nanomaterials* **9**, 374 (2019).

[11] U.P. Tyagi, P. Goswami, arXiv:2506.16867 (2025).

[12] Y. Qiu, K. Yan, S. Yang, L. Jin, H. Deng, W. Li, *ACS Nano* **4**, 6515 (2010).

[13] M.S.A. Bhuyan, M.N. Uddin, M.M. Islam, F.A. Bipasha, S.S. Hossain, *Int. Nano Lett.* **6**, 65 (2016).

[14] S. Goenka, V. Sant, S. Sant, *J. Control. Release* **173**, 75 (2014).

[15] A. Du, Y.H. Ng, N.J. Bell, Z. Zhu, R. Amal, S.C. Smith, *J. Phys. Chem. Lett.* **2**, 894 (2011).

[16] R. Long, N.J. English, O.V. Prezhdo, *J. Am. Chem. Soc.* **134**, 14238 (2012).

[17] J. Sivek, O. Leenaerts, B. Partoens, F. Peeters, arXiv:1301.3654 (2013).

[18] N. Yang, Y. Liu, H. Wen, Z. Tang, H. Zhao, Y. Li, D. Wang, *ACS Nano* **7**, 1504 (2013).

[19] R. Long, *J Phys. Chem. Lett.* **4**, 1340 (2013).

[20] M. Rojas, E. Leiva, *Phys. Rev. B* **76**, 155415 (2007).

[21] N. Allouche, B. Boudjema, R. Daira, F. Bayansal, *Acta Phys. Pol. A* **145**, 169 (2024).

[22] M. Segall, P.J.D. Lindan, M.J. Probert, C.J. Pickard, P.J. Hasnip, S.J. Clark, M.C. Payne, *J. Phys. Condens. Matter* **14**, 2717 (2002).

[23] A. Yahaya, W. Yahya, A. Ahmed, A. Sholagberu, *Acta Phys. Pol. A* **145**, 194 (2024).

[24] J.P. Perdew, K. Burke, M. Ernzerhof, *Phys. Rev. Lett.* **77**, 3765 (1996).

[25] P.E. Blöchl, *Phys. Rev. B* **50**, 17953 (1994).

[26] S.L. Dudarev, G.A. Botton, S.Y. Savrasov, C. Humphreys, A.P. Sutton, *Phys. Rev. B* **57**, 1505 (1998).

[27] M. Datteo, Ph.D. Thesis, University of Milano-Bicocca, 2020.

[28] A. Tkatchenko, M. Scheffler, *Phys. Rev. Lett.* **102**, 073005 (2009).

[29] Y.-X. Yuan, *IMA J. Numer. Anal.* **11**, 325 (1991).

[30] H. Etea, K. Nigussa, arXiv:2305.02798 (2023).

[31] F.A. Rasmussen, K.S. Thygesen, *J. Phys. Chem. C* **119**, 13169 (2015).

[32] R.C. Andrew, R.E. Mapasha, A.M. Ukpong, N. Chetty, *Phys. Rev. B* **85**, 125428 (2012).

[33] V.G. Tyuterev N. Vast, *Comput. Mater. Sci.* **38**, 350 (2006).

[34] C.-H. Zhou, Q. Xu, S.-T. Li, X. Zhao, *J. Adv. Dielectr.* **2**, 1250004 (2012).

[35] P. Wang, C. Jia, Y. Huang, X. Duan, *Matter* **4**, 552 (2021).

[36] G.V. Pushkarev, V.G. Mazurenko, V.V. Mazurenko, D.W. Boukhvalov, *J. Phys. Chem. C* **127**, 8148 (2023).

[37] W. Zhou, J. Chen, Z. Yang, J. Liu, F. Ouyang, *Phys. Rev. B* **99**, 075160 (2019).

[38] Y. Tang, Q. Liu, J. Lei, M. Zhang, H. Yang, M. Duan, X. Ma, T. Song, *Mater. Res. Express* **9**, 105502 (2022).

[39] E. Song, Y. Zhu, *Nanosci. Nanotechnol. Lett.* **5**, 198 (2013).

[40] S. Shan, W. Liu, W. Zou, R. Chen, C. Hu, *Acta Phys. Pol. A* **145**, 157 (2024).

[41] P.N. Gillespie, N. Martsinovich, *ACS Appl. Mater. Interfaces* **11**, 31909 (2019).

[42] W. Fu, Y. Li, M.-S. Chen, Y. Hu, B. Liu, K. Zhang, C. Zhan, M. Zhang, Z. Shen, *J. Power Sources* **468**, 228363 (2020).

[43] D. Wang, D. Choi, J. Li et al., *ACS Nano* **3**, 907 (2009).

[44] Y. Cen, Y. Yao, Q. Xu, Z. Xia, R.D. Sisson, J. Liang, *RSC Adv.* **6**, 66971 (2016).

[45] S. Ding, J.S. Chen, D. Luan, F.Y.C. Boey, S. Madhavi, X.W.D. Lou, *Chem. Commun.* **47**, 5780 (2011).

[46] S. Umrao, S. Abraham, F. Theil et al., *RSC Adv.* **4**, 59890 (2014).

[47] H. Zhang, X. Lv, Y. Li, Y. Wang, J. Li, *ACS Nano* **4**, 380 (2010).

[48] B. Qiu, Y. Zhou, Y. Ma, X. Yang, W. Sheng, M. Xing, J. Zhang, *Sci. Rep.* **5**, 8591 (2015).

[49] X. Liao, R. Lu, L. Xia, Q. Liu, H. Wang, K. Zhao, Z. Wang, Y. Zhao et al., *Energy Environ. Mater.* **5**, 157 (2022).

[50] L. Xu, W.-Q. Huang, L.-L. Wang, G.-F. Huang, *ACS Appl. Mater. Interfaces* **6**, 20350 (2014).

[51] Y.-C. Yang, L. Xu, W.-Q. Huang, C.-Y. Luo, G.-F. Huang, P. Peng, *J. Phys. Chem. C* **119**, 19095 (2015).

[52] X. Li, H. Gao, G. Liu, *Comput. Theor. Chem.* **1025**, 30 (2013).

[53] W. Xuan, N. Yang, J. Luo, R. Wang, H. Yang, G. Jin, *Appl. Phys. A* **129**, 88 (2023).

[54] B. Zhou, K. Jiang, L. Shang, J. Zhang, Y. Li, L. Zhu, S.-J. Gong, Z. Hu, J. Chuacd, *J. Mater. Chem. C* **8**, 11160 (2020).

[55] M. Ahmed, A. Bakar, A. Quader, R.A. Ahmad, S.M. Ramay, *Chem. Phys.* **581**, 112260 (2024).

[56] A. Fereidoon, S. Aleaghaee, I. Taraghi, *Comput. Mater. Sci.* **102**, 220 (2015).

[57] Q. Peng, K. Hu, B. Sa, J. Zhou, B. Wu, X. Hou, Z. Sun *Nano Rese.* **10**, 3136 (2017).